

# Atomistic study of edge and screw $\langle c + a \rangle$ dislocations in magnesium

T. Nogaret<sup>a,\*</sup>, W.A. Curtin<sup>a</sup>, J.A. Yasi<sup>b</sup>, L.G. Hector Jr<sup>c</sup>, D.R. Trinkle<sup>d</sup>

<sup>a</sup> Division of Engineering, Brown University, Providence, RI 02912, USA

<sup>b</sup> Department of Physics, University of Illinois, Urbana-Champaign, Urbana, IL 61801, USA

<sup>c</sup> General Motors R&D Center, 30500 Mound Road, Warren, MI 48090-9055, USA

<sup>d</sup> Department of Material Science and Engineering, University of Illinois, Urbana-Champaign, Urbana, IL 61801, USA

Received 26 February 2010; received in revised form 6 April 2010; accepted 11 April 2010

Available online 17 May 2010

## Abstract

The gamma surfaces in the pyramidal I  $\{1 - 1 0 1\}$  and II  $\{1 1 - 2 2\}$  planes for hexagonal close packed Mg have been calculated using two embedded-atom-method potentials and by ab initio methods, and reasonable agreement is obtained for key stacking fault energies. Screw and edge  $\langle c + a \rangle$  dislocation core structures and Peierls stresses at 0 K and finite temperature have been examined using the embedded-atom-method potentials. Screw  $\langle c + a \rangle$  dislocations glide in the  $\{1 - 1 0 1\}$  pyramidal plane I, and in the prism plane for larger stresses, but not in the  $\{1 1 - 2 2\}$  plane as observed in experiments. However, the preference for pyramidal I glide correlates well with the gamma surfaces. New low energy edge  $\langle c + a \rangle$  dislocation cores were found in addition to the sessile Type I and Type III cores observed in previous simulations while the Type II core was not observed. The lowest energy core is a glissile core that lies in the  $\{1 1 - 2 2\}$  plane and has a 3 nm long  $\{1 1 - 2 1\}$  twin embryo, rather than the sessile Type III core found in previous simulations. As the temperature increases from 0 to 300 K, the Peierls stresses in compression/tension drop from  $-80$  MPa/ $+140$  MPa and  $-140$  MPa/ $+220$  MPa for the most glissile screw and edge dislocations to  $-5/+2.5$  MPa and  $-27/+5$  MPa, and dislocation glide changes from kink motion to face-centered-cubic-like motion. At 300 K and under an applied stress, almost all the edge cores found at low temperature transform into a glissile core denoted IT, which glides at low stresses. Thus, at 300 K both screw and edge  $\langle c + a \rangle$  dislocations were found to glide at stresses smaller than the  $\sim 40$  MPa measured experimentally.

© 2010 Acta Materialia Inc. Published by Elsevier Ltd. All rights reserved.

**Keywords:** Magnesium; Dislocation; Twinning; Ab initio electron theory; Molecular dynamics

## 1. Introduction

Magnesium alloys are increasingly being used, or considered for use, in structural components due to their low density. However, Mg alloys suffer from poor formability due to the underlying hexagonal close packed (hcp) structure of Mg, which creates high anisotropy in the plastic deformation. Deformation along the  $\langle a \rangle$  axis is easy, occurring at very low stresses, with much higher stresses required to activate deformation modes accommodating deformation along the  $\langle c \rangle$  axis. The deformation along the  $\langle c \rangle$  axis is complicated and can involve  $\langle c + a \rangle$  and twinning dislocations, and a clear understanding is a challenge for mate-

rials scientists. Atomistic level modeling of dislocation structures and motion is one avenue through which insight into the deformation modes can be obtained. To this end,  $\langle c + a \rangle$  dislocations have been studied at 0 K for several decades using simple interatomic potentials [1–9] and embedded atom method (EAM) potential [12,13], but the potentials were usually fitted to hcp zirconium or used very small computational cells of 9000 atoms with only 1000 atoms free to relax, which is too small to accurately capture the extended  $\langle c + a \rangle$  dislocations. Only Liang and Bacon [7–9] used a pair potential designed for Mg, but that study was limited by the small cell size. Ando et al. [11] performed also simulations at finite temperature, but they used a very small cell and a Zr Lennard–Jones potential.

In this paper, we study the  $\langle c + a \rangle$  dislocations using improved Mg EAM potentials [14,15] and large scale

\* Corresponding author. Tel.: +1 401 863 2674.

E-mail address: [thomas\\_nogaret@brown.edu](mailto:thomas_nogaret@brown.edu) (T. Nogaret).

simulations at 0 K and finite temperature. We have recently shown that these EAM potentials have more realistic properties for basal and prism  $\langle a \rangle$  dislocations, especially the Sun potential that is in good agreement with ab initio calculations [16]. Here we investigate  $\langle c + a \rangle$  dislocation core structures in the hcp pyramidal planes and correlate the structures and Peierls stresses to selected gamma surfaces calculated by both EAM potentials and ab initio calculations. We find a wide range of stable core structures that transform among one another under applied loading, with generally high Peierls stresses in the range of 80–220 MPa required for glide at  $T = 0$  K. The more glissile stable screw  $\langle c + a \rangle$  core lies and glides in the pyramidal I  $\{1 - 1 0 1\}$  plane, but not in the pyramidal II  $\{1 1 - 2 2\}$  plane as in experiments. The most stable and glissile edge  $\langle c + a \rangle$  dislocation core is a glissile core lying in the  $\{1 1 - 2 2\}$  plane with a 3 nm long  $\{1 1 - 2 1\}$  twin embryo. As the temperature increases up to 300 K, the associated Peierls stresses decrease to the range of 2.5–30 MPa.

This paper is organized as follows. In Section 2, we describe the simulation geometries and methods. In Section 3, we present the gamma surfaces for  $\{1 - 1 0 1\}$  and  $\{1 1 - 2 2\}$  pyramidal planes. Sections 4 and 5 present the results for the structure and glide of screw and edge  $\langle c + a \rangle$  dislocations in pyramidal planes, respectively. In Section 6, we present the results for screw and edge  $\langle c + a \rangle$  dislocations at finite temperature. We discuss our results and conclude in Section 7.

## 2. Simulation geometries and methods

For molecular dynamics modeling, EAM potentials developed by Sun et al. [15] and Liu et al. [14] are used. Molecular calculations are carried out using the LAMMPS code [17]. The ab initio calculations are performed with VASP [18,19], a planewave-based density-functional theory code using Vanderbilt-type ultrasoft pseudopotentials [20,21] and the generalized-gradient approximation of Perdew and Wang for the exchange–correlation potential [22]. The 3s states of Mg are treated as valence electrons, while the other electron states are frozen in their core configurations; a planewave energy cutoff of 138 eV is used throughout the calculations. The choice of exchange–correlation potential, pseudopotential, and planewave cutoff are made by comparing lattice and elastic constants and phonons spectra with experimental values; our selection produces errors of 0.7% for lattice constants, 5% for bulk modulus, and 3% for phonon frequencies.

The simulation cell uses a  $Z$  coordinate normal to the glide plane and a  $Y$  coordinate parallel to the  $\langle c + a \rangle$  Burgers vector  $1/3[1 1 - 2 3]$ . Gamma surfaces are computed as follows. The surfaces along the  $Z$  direction are free and periodic boundary conditions are applied along  $X$  and  $Y$ . The upper half of the crystal ( $Z > 0$ ) is shifted by a translation vector  $\mathbf{t} = \mathbf{dX} + \mathbf{dY}$  in the  $X$ – $Y$  plane. All atoms are held fixed in the  $X$  and  $Y$  directions but are allowed to relax along the  $Z$  direction. The gamma surface then corresponds to the

relaxed energy versus translation  $\mathbf{t}$ . The Sun and Liu EAM potential gamma surfaces in pyramidal I  $\{1 - 1 0 1\}$  and II  $\{1 1 - 2 2\}$  planes are performed using perfect crystals of dimensions  $(1 \times 1 \times 46)$  and  $(1 \times 1 \times 40)$  unit cells. The “quench method” is used to find the minimum energy [23], with convergence corresponding to individual forces below  $10^{-6}$  eV  $\text{\AA}^{-1}$  on all atoms near the surfaces within the EAM potential cut-off radius and below  $10^{-8}$  eV  $\text{\AA}^{-1}$  on all interior atoms. The ab initio gamma surface calculations are performed using  $1 \times 1 \times 10$  (40 atoms total) periodic supercells for both  $\{1 1 - 2 2\}$  and  $\{1 - 1 1 0\}$  generalized stacking fault surfaces. We take advantage of mirror symmetry when sampling the full stacking fault surface: for  $\{1 1 - 2 2\}$ , we perform  $7 \times 11$  calculations in the plane  $(1/2[1 - 1 0 0] \times 1/3[1 1 - 2 3])$  and for  $\{1 - 1 0 1\}$   $7 \times 7$  calculations in the plane  $(1/2[1 - 1 0 2] \times 1/6[1 1 - 2 0])$ . The  $16 \times 10$   $\{1 1 - 2 2\}$  and  $9 \times 16$   $\{1 - 1 1 0\}$   $k$ -point meshes are integrated with Methfessel–Paxton smearing of 0.5 eV. All forces are relaxed to within 5 meV  $\text{\AA}^{-1}$ , corresponding to an energy error of less than 1%.

For simulations at 0 K, dislocations are created in the center of a perfect crystal having dimensions of one unit cell length along the line direction and  $\sim 100$  nm in both the dislocation glide and  $Z$  directions at 0 K. The edge dislocation is created by removing atoms within a band of width  $b$  (where  $b = \|\langle c + a \rangle\|$ ,  $a$  and  $c$  being the lattice parameters, with  $a = 3.184$   $\text{\AA}$  and  $c/a = 1.628$  for Sun potential,  $a = 3.196$   $\text{\AA}$  and  $c/a = 1.623$  for Liu potential) and with negative  $Z$  coordinates from the perfect crystal. Initial structures for both edge and screw dislocations are usually dislocations dissociated in the glide plane by  $0$ – $8a$  in two  $1/2\langle c + a \rangle$  dislocations generated by displacing all atoms according to the Volterra solution. Boundary conditions are periodic in the dislocation line direction, traction free on the surface normal to the glide direction, and mixed boundary conditions on the surface normal to the  $Z$  direction. Specifically, atoms located within the EAM potential cut-off radius of the  $Z$  surfaces are fixed in the  $Z$  direction but free to relax along the  $X$  and  $Y$  directions, and have applied forces in  $Y$  so as to create shear stresses  $\sigma_{YZ}$ . With our crystal orientation, the application of a positive (resp. negative) shear stress  $\sigma_{YZ}$  induces a tension (resp. compression) along the  $[0 0 0 1]$  direction. We use the same methodology as for gamma surfaces and the applied stress increments are always smaller than 10% of the Peierls stress; thus the exact value of the Peierls stress at 0 K is between 0.9 and 1.0 times the Peierls stresses we quote here.

For simulations at finite temperature, we use as initial configurations the relaxed cores obtained in the study at 0 K but placed in a smaller simulation cell. Specifically, we use dislocation line lengths of 3.64 nm and 3.86 nm for the screw and edge dislocations and decrease the box size to 40 nm in the  $Z$  direction and use a dislocation glide distance of 80 nm and 40 nm for screw and edge dislocation. A longer glide distance is used for screw dislocation because side effects are seen with smaller boxes: the low

Peierls stress combined with the thermal noise at 300 K makes the dislocation undulate and glide slightly and, since the image forces are not zero when the dislocation is not at the center of the box, the dislocation is attracted toward one of the free surfaces.

We find that extreme care must be taken to perform simulations at finite temperature under well-controlled shear stresses. Starting at  $T = 0$  K, the temperature is increased by  $15 \text{ K ps}^{-1}$  up to 300 K. As the temperature is increased, undesired shear stress waves with amplitude 20–40 MPa are created in the crystal. The NPT ensemble in LAMMPS [17] allows for control of the pressures but not the shear stresses. In order to maintain the shear stresses to within  $\pm 5$  MPa of the target applied stresses, we designed an ad hoc procedure as follows. We simultaneously used two Nose/Hoover NPT thermostat/barostats. For both, the pressure damping and drag parameters were 0.1 and 1.0, respectively. The temperature damping parameters in the two thermostats were 0.1 and 1.0. We also simultaneously apply atom velocity rescaling with “window” and “fraction” parameters equal to 1.0. Then, 10 ps after the target temperature is reached, temperature rescaling is eliminated. After another 10 ps, the second Nose/Hoover thermostat/barostat is eliminated. After another 10 ps, we begin application of a shear stress that increases continuously at a stress rate of  $0.5\text{--}1.0 \text{ MPa ps}^{-1}$ . To obtain crystals at 5, 77, 150 and 200 K, we start from the state that previously equilibrated at 300 K and use the dual thermostat/barostat and atom velocity rescaling strategy to cool the system down to the target temperature. The temperature, applied stress, and measured  $\sigma_{11}$ ,  $\sigma_{12}$  and  $\sigma_{23}$  as functions of temperature are shown in Fig. 1 for a typical simulation. All the pressure components are zero within  $\sim \pm 5$  MPa and the  $\sigma_{23}$  is fluctuating by less than  $\sim \pm 5$  MPa around the applied stress.

The critical resolved shear stress (CRSS) is determined by viewing the motion of the dislocation line normal to the slip plane. Below the CRSS, the dislocation is immobile

and perfectly straight (see Fig. 1, inset at 50 MPa). Above the CRSS, the dislocation moves either by a kink nucleation–propagation process (see Fig. 1, inset at 55 MPa) at low temperature, or it undulates at higher temperature when the Peierls stresses is low. The CRSS is taken as the minimum stress for which the dislocation glides over a distance  $2b = 2\|c + a\| \sim 12.2 \text{ \AA}$ . We checked the validity of this measure in some simulations by holding the applied stress constant around the CRSS value. Due to the  $\sim \pm 5$  MPa internal stress fluctuations, the dislocation would glide when the internal stress was above the CRSS and remained fixed when the internal stress was below the CRSS.

### 3. Gamma surfaces for pyramidal I $\{1\ 0\ -1\}$ and pyramidal II $\{1\ 1\ -2\}$ slip

The pyramidal I  $\{1\ -1\ 0\}$  gamma surface for the Sun potential and ab initio calculation is shown in Fig. 2. The  $\langle c + a \rangle = 1/3[2\ -1\ -1\ -3]$  Burgers vectors and the minimum energy paths to form this vector are indicated in the figure. Two stable stacking faults, denoted F1 and F2, and three unstable stacking faults denoted U1, U2 and U3, exist on the Sun minimum energy path. All of these points are also found with the Liu potential and the na56 potential [7], but the stable F2 and unstable U3 SFs are absent in the ab initio gamma surface. Table 1 shows the stable and unstable SF energies for the Sun and Liu potentials and the ab initio calculation. The unstable SFs along the  $\langle a \rangle = 1/3[1\ 1\ -2\ 0]$  direction are 266, 226 and  $310 \text{ mJ m}^{-2}$  for Sun and Liu potentials and ab initio, values about  $100 \text{ mJ m}^{-2}$  larger than those in the prism plane [16]. Consequently,  $\langle a \rangle$  dislocation glide is expected to be easier in the prism plane than in the pyramidal I plane. The stable SFs F1 and F2 along the  $\langle c + a \rangle$  minimum energy path have high energies of 240 and  $118 \text{ mJ m}^{-2}$  for the Sun potential and, similarly, 225 and  $121 \text{ mJ m}^{-2}$ , for the Liu potential, with the F1 values

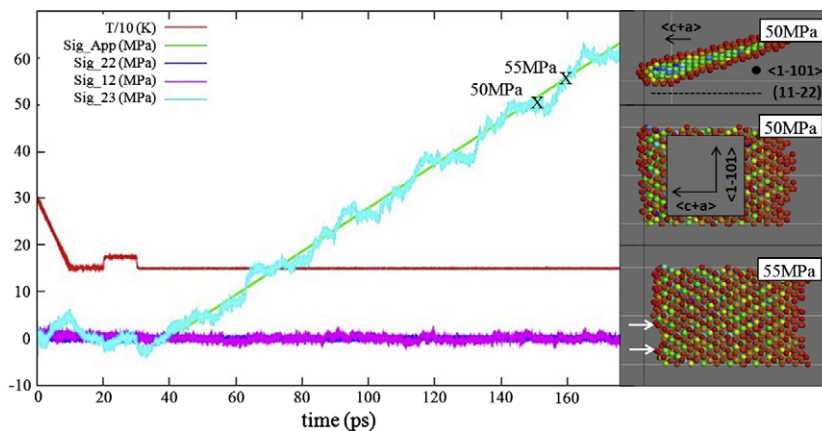


Fig. 1. Temperature and stress (applied stress,  $\sigma_{11}$ ,  $\sigma_{12}$ , and  $\sigma_{23}$ ) versus time during loading of a simulation cell containing a pyramidal II  $\{1\ 1\ -2\}$  edge  $\langle c + a \rangle$  dislocation at 150 K. Inset: dislocation configurations below and above the CRSS (50 MPa: side and top views show that the left partial of the dislocation is pinned, remaining straight and immobile; 55 MPa: top view shows that the previously pinned partial glides by kink nucleation and propagation).

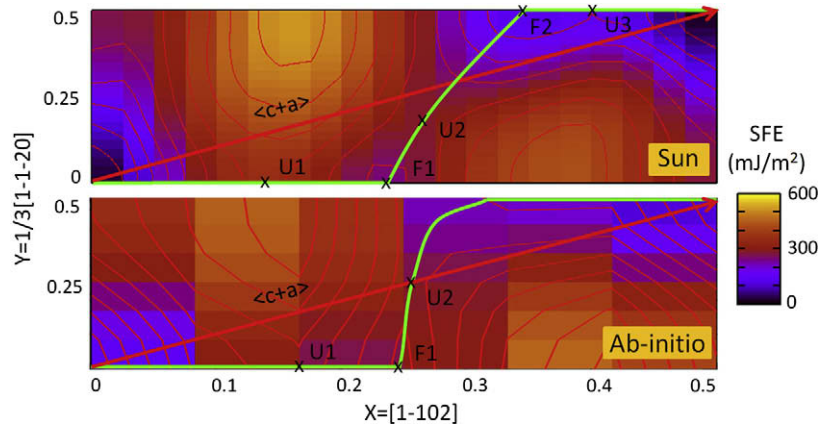


Fig. 2. Projection of  $\{1 -1 0 1\}$  plane gamma surface with  $50 \text{ mJ m}^{-2}$  isolines for the Sun potential (a) and ab initio calculations (b). The  $\langle c + a \rangle = 1/3[2 -1 -1 -3]$  Burgers vector and the minimum energy path to form this vector are indicated in red and green on the figure. F1 and F2 indicate the two stable SFs (if present) and U1, U2 and U3 the three unstable SFEs.

Table 1

Stable and unstable stacking fault energies (SFEs) in  $\text{mJ m}^{-2}$  for the pyramidal planes I  $\{1 -1 0 1\}$  and II  $\{1 1 -2 2\}$ , for Sun and Liu potentials and ab initio calculations. For the  $\{1 -1 0 1\}$  plane, the unstable SFE along the  $\langle a \rangle$  direction, the stable (F1 and F2) and unstable (U1, U2, and U3) SFEs along the  $\langle c + a \rangle$  minimum energy path are given if present. For the  $\{1 1 -2 2\}$  plane, the stable and unstable SFEs (V1 and V2) along the  $\langle c + a \rangle$  minimum energy path are given if present. The ratio U1/V1 of the two maximal unstable SFEs along the  $\langle c + a \rangle$  minimum path in pyramidal I and II planes is also shown.

Stacking fault energy ( $\text{mJ m}^{-2}$ )	$\{1 -1 0 1\}$ plane						$\{1 1 -2 2\}$ plane			Ratio U1/V1
	$\langle a \rangle$ min. path		$\langle c + a \rangle$ min. path				$\langle c + a \rangle$ min. path			
	Unstable	Unstable			Stable		Stable	Unstable		
		U1	U2	U3	F1	F2		V2	V1	
Ab initio	310	335	238	×	180	×	236	243	485	0.69
Sun EAM	266	356	285	149	240	118	×	×	640	0.56
Liu EAM	226	300	261	164	225	121	198	206	505	0.59

higher than the  $180 \text{ mJ m}^{-2}$  obtained in the ab initio calculation. However, all of these stable SFs are very stable: the lowest energy barriers to escape from these stable SFs are  $31\text{--}58 \text{ mJ m}^{-2}$ , and the ab initio F1 SF is the most stable. The unstable SFEs U1 along the  $\{1 -1 0 1\}$   $\langle c + a \rangle$  minimum energy path are high, above  $300 \text{ mJ m}^{-2}$  in all cases, and  $\sim 100\text{--}200 \text{ mJ m}^{-2}$  larger than the values obtained along the  $\{1 -1 0 0\}$   $\langle a \rangle$  minimum energy path [16]. Consequently, higher Peierls stresses are expected for pyramidal I  $\langle c + a \rangle$  dislocations than for prism  $\langle a \rangle$  dislocations.

The cross-section of the  $\{1 1 -2 2\}$  pyramidal II plane gamma surface along the  $1/3[1 1 -2 3]$  direction is shown in Fig. 3 for Sun and Liu EAM potentials and ab initio calculation. The Liu potential and the ab initio gamma surfaces have a stable SF at 0.25 and 0.33  $\langle c + a \rangle$  with energies of 198 and  $236 \text{ mJ m}^{-2}$ , respectively, but having a shallow minimum (8 and  $7 \text{ mJ m}^{-2}$ ), while the Sun potential gamma surface does not have a minimum. The na56 potential also has a stable SF in this case [7]. The maximal unstable SFEs along the  $\langle c + a \rangle$  direction (labeled V1) are much larger than in the  $\{1 -1 0 1\}$  plane, 505 and  $485 \text{ mJ m}^{-2}$  for the Liu potential and ab initio calculations, and  $640 \text{ mJ m}^{-2}$  for the Sun potential. The glide of  $\langle c + a \rangle$

dislocations is thus expected to be easier in the pyramidal I plane than in the pyramidal II plane.

#### 4. $\langle c + a \rangle$ dislocations at 0 K

Unless otherwise noted, the results for  $\langle c + a \rangle$  dislocations are shown for the Sun et al. potential. Limited studies

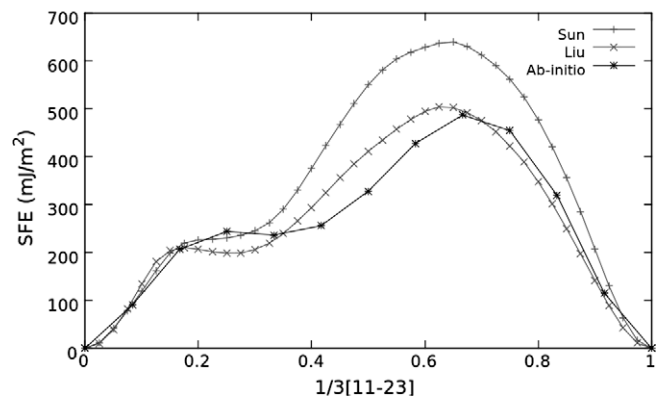


Fig. 3. Cross-section of the  $\{1 1 -2 2\}$  pyramidal II plane gamma surface along the  $1/3[1 1 -2 3]$  direction for Sun and Liu EAM potentials and ab initio calculation.

using the potential by Liu et al. are noted when appropriate.

#### 4.1. Screw dislocations

Screw  $\langle c + a \rangle$  dislocations can potentially glide in six different planes as shown in the upper right of Fig. 4: one prism  $\{1 -1 0 0\}$  plane, one pyramidal II plane  $\{1 1 -2 2\}$ , two pyramidal I planes  $\{1 -1 0 1\}$ , and two  $\{1 1 -2 1\}$  planes. We thus use four different crystal orientations to study the screw  $\langle c + a \rangle$  dislocation. Screw dislocations are usually introduced as dissociated into two  $\frac{1}{2}\langle c + a \rangle$  screw dislocations separated by  $0-6a$  along the chosen slip plane. After relaxation at 0 K, three different kinds of cores, labeled P0, PI and PII, form, as shown in Fig. 4 using potential energy to visualize their structures. The P0 core (Fig. 4a) spreads  $\sim 6-7a$  in the two  $\{1 1 -2 1\}$  planes. This core is observed when the core is introduced un-dissociated, or dissociated in the  $(1 -1 0 0)$  or the  $\{1 1 -2 1\}$  plane. The PI core is obtained when the dislocation is initially introduced as dissociated in the  $\{1 -1 0 1\}$  pyramidal I planes, where it dissociates further to  $\sim 8a$  (Fig. 4b). This core exhibits an out-of-plane partial dislocation on the left side. The PII core is obtained when the initial dislocation is introduced dissociated on the  $(1 1 -2 2)$  pyramidal II plane and lies on the  $(1 1 -2 2)$  plane as a relatively compact core with dissociation distance  $\sim 4a$  (Fig. 4c).

To compare the core energies of these different dislocation core structures, we measure the energy  $E(r)$  of all

atoms contained within a cylindrical region of radius  $r$  centered on the dislocation line. Beyond a rough “core radius” of  $r_C$  of twice the dissociation distance, this energy per unit line length scales as  $E(r) = E(r_C) + A \ln(r/r_C)$ . Since all these cores have the same Burger’s vector, they have the same constant  $A$  and we then can compare their respective values of  $E(r_C)$ . By this method, the P0 core has the lowest energy, with the PI and PII core energies being  $0.07 \text{ eV b}^{-1}$  and  $0.17 \text{ eV b}^{-1}$  higher.

We calculated the CRSS at 0 K for each core, as summarized in Table 2. The Peierls barrier depends on the sign of the shear stress. We label as “negative” a shear stress that induces compression along the  $\langle c \rangle$  axis, while a “positive” shear stress induces tension. For negative and positive applied stresses, the PII core has Peierls stresses lower than  $-220 \text{ MPa}$  and larger than  $+170 \text{ MPa}$ , respectively, when the  $Z$  axis is normal to the  $(1 1 -2 2)$  plane. Beyond these stresses, the dislocation cross-slips onto the  $(0 1 -1 -1)$  plane to become a PI core, where it glides. The PI core glides for stresses of  $-140 \text{ MPa}$  and  $+80 \text{ MPa}$  when  $Z$  is normal to the  $(0 1 -1 -1)$  plane. As the stress approaches the Peierls barrier, the right part of the PI core glides some angstroms but the left part remains sessile until the Peierls stresses are reached. Similar behavior was observed for the P0 and PI cores using the Liu potential.

The P0 core has Peierls stresses of  $\pm 200 \text{ MPa}$  when  $Z$  is normal to the  $(1 -1 0 0)$  plane. As the negative applied stress increases, the symmetric core that initially lies in

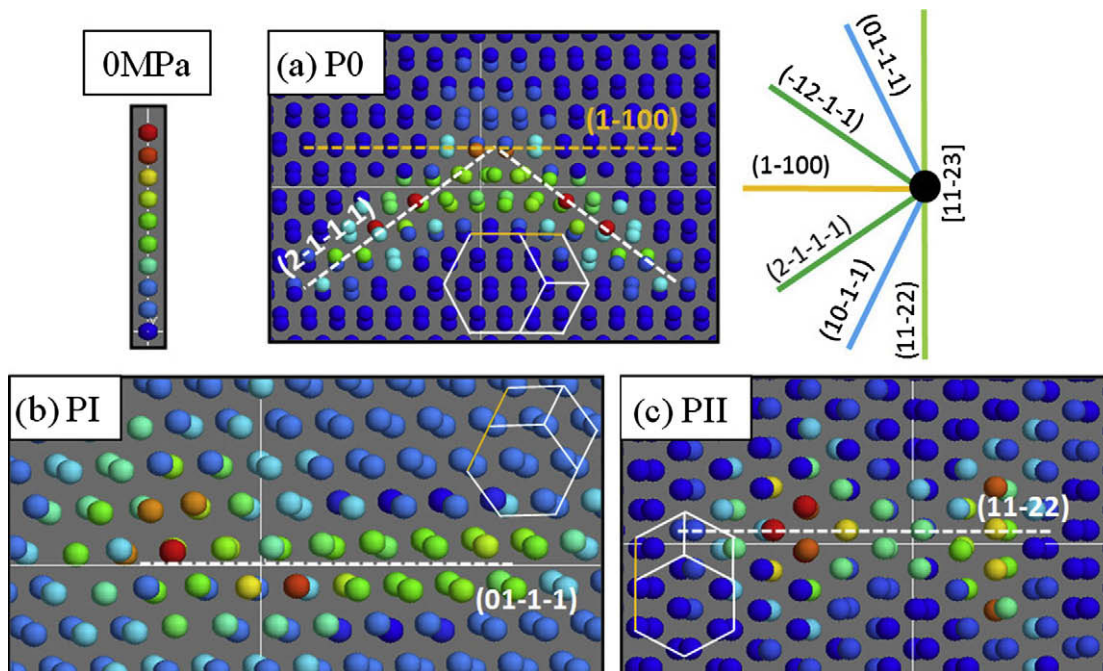


Fig. 4. Screw  $\langle c + a \rangle$  dislocation cores predicted at 0 MPa using the Sun potential. (a) P0 core with  $Z$  normal to  $(1 -1 0 0)$ ; (b) PI core with  $Z$  normal to  $(0 1 -1 -1)$ ; (c) PII core with  $Z$  normal to  $(1 1 -2 2)$ . Atom colors show potential energy relative to perfect crystal Mg, ranging from  $-0.03 \text{ eV}$  (dark blue) to  $+0.1 \text{ eV}$  (red). The hcp unit cell is shown on every figure with the  $(1 -1 0 0)$  prism plane trace in orange. The different glide planes that contain the  $\langle c + a \rangle$  Burgers vector are also shown. (For interpretation of the references to color in this figure legend, the reader is referred to the web version of this article.)

Table 2

Screw and edge  $\langle c+a \rangle$  dislocations for Sun potential: transformations and critical resolved shear stresses (CRSS) at 0 K and 300 K. Also shown is  $\Delta E_c = (\text{dislocation core energy}) - (\text{energy of lowest energy core})$  at 0 K. With our crystal orientation, the negative and positive stresses induce respectively compression and tension along the  $\langle c \rangle$  axis.

Temperature	0 K				300 K				
	$\Delta E_c$ (eV b <sup>-1</sup> )	Negative CRSS (MPa)		Positive CRSS (MPa)		Negative CRSS (MPa)		Positive CRSS (MPa)	
Screw $\langle c+a \rangle$	$E-E_{P0}$								
{1 -1 0 0} P0	0	-200	Glide	+200	{1 -1 0 0} Glide	-50	Glide	+50	Glide
{1 1 -2 1} P0	0	-280	→{1 -1 0 0} P0	+280	→{1 1 -2 1} Twin	-85	→{1 -1 0 1} PI	+60	→{1 -1 0 1} PI
{1 -1 0 1} PI	+0.07	-140	Glide	+80	Glide	-5	Glide	+2.5	Glide
{1 1 -2 2} PII	+0.17	-200	→{1 -1 0 1} PI	+170	→{1 -1 0 1} PI	-30	→{1 -1 0 1} PI	+30	→{1 -1 0 1} PI
Edge $\langle c+a \rangle$	$E-E_{IT}$								
{1 1 -2 2} I	+0.40	-250	→IC + Vac	+140	→IT	0	→IT (200 K)	0	→IT (200 K)
{1 1 -2 2} IC	+0.05	-160	Glide	+220	Glide	-27	Glide	+27	Glide
{1 1 -2 2} IT	+0.00	-300	→ $\langle c \rangle + \langle a \rangle$	+220	Glide	-27	Glide	+5	Glide
{1 1 -2 2} ITC	Unstable	-300	→ $\langle c \rangle + \langle a \rangle$	×	→IT	×	×	×	×
{1 1 -2 2} III	+0.02	-300	→ $\langle c \rangle + \langle a \rangle$	+100	→IIIT	-90	→IT	+40	→IT
{1 1 -2 2} III'	+0.12	-300	→IIIC	+100	→IIIT	-300	→ $\langle c \rangle + \langle a \rangle$	+40	→IT
{1 1 -2 2} IIIC	+0.26	-140	Glide	+140	→IIIT	-45	Glide	+45	Glide
{1 1 -2 2} IIIT	+0.26	-40	→III	+220	→{1 1 -2 1} Twin	0	→IT (250 K)	0	→IT (250 K)

two {1 1 -2 1} planes spreads more and more on the left in the (2 -1 -1 -1) plane and then transforms into a compact core in the prism plane with a (2 -1 -1 -1) twin embryo of about  $12a$  in length on the left, as seen in Fig. 5a. A similar situation occurs as the positive applied stress increases, with the symmetric core in the two {1 1 -2 1} planes spreading more on the right in the (-1 2 -1 -1) plane and transforming into a compact core in the prism plane with a (-1 2 -1 -1) twin embryo of about  $12a$  in length on the right. When  $Z$  is normal to the (-1 2 -1 -1) plane, for negative stresses the P0 core spreads on the left in the (2 -1 -1 -1) plane and then glides in the prism plane at a stress of -280 MPa, and for positive stresses it extends as a (-1 2 -1 -1) twin when the stress reaches +280 MPa, as shown in Fig. 5b.

The main results for screw dislocations as found using the Sun et al. potential are summarized in Table 2, which shows the core energies, and the critical resolved shear stresses for either glide or transformation.

#### 4.2. Edge dislocations

In previous simulations, three type of edge  $\langle c+a \rangle$  cores were observed with various Mg and Zr potentials [1,3,8–

13]. In the present simulations, the Type II core that consists of two  $\frac{1}{2} \langle c+a \rangle$  partials lying in the (1 1 -2 2) plane was not observed, even when using initial configurations with dissociated partials separated by up to  $8a$ . However, we do observed the Type I and III cores, as well as 3 Type I and 3 Type III variations described below.

The Type I core family is characterized by a compact core lying in a single (1 1 -2 2) plane. The Type I core is shown for Sun potential in Fig. 6a and is obtained by relaxing a compact core created using the elastic Volterra solution shown in Fig. 6b. The Type I core is composed of a zone in compression around the red atom, a zone in tension near the yellow atoms, and a (1 1 -2 1) twin embryo on the right. This core has a very high energy,  $+0.40 \text{ eV b}^{-1}$  as compared to the core we denote IT that is described below.

At a positive shear stress of +140 MPa, the Type I core transforms into a dislocation core we denote IT that is shown in Fig. 6c at 0 MPa. The IT core has the lowest energy among all the edge  $\langle c+a \rangle$  dislocation cores observed here. The shift to the right of atoms marked “x” in Fig. 6a into the position in Fig. 6c allows the release of the compression and tension zones found in the original Type I core. The IT core can be formed “by hand” by moving the red atom of the Type I core (Fig. 6a) into the “hole”

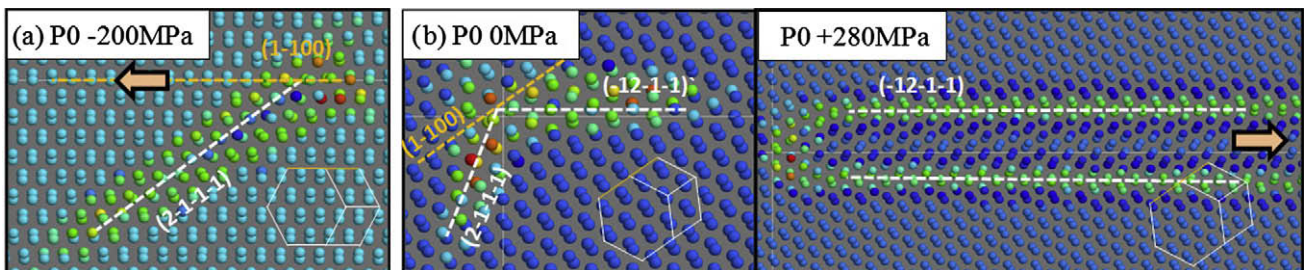


Fig. 5. Screw  $\langle c+a \rangle$  dislocation cores using the Sun potential, at the 0 K Peierls stress. (a) P0 core with  $Z$  normal to (1 -1 0 0) at -200 MPa; (b) P0 core with  $Z$  normal to (-1 2 -1 -1) at +280 MPa. Atom colors show potential energy relative to perfect crystal Mg, ranging from -0.03 eV (dark blue) to +0.1 eV (red). (For interpretation of the references to color in this figure legend, the reader is referred to the web version of this article.)

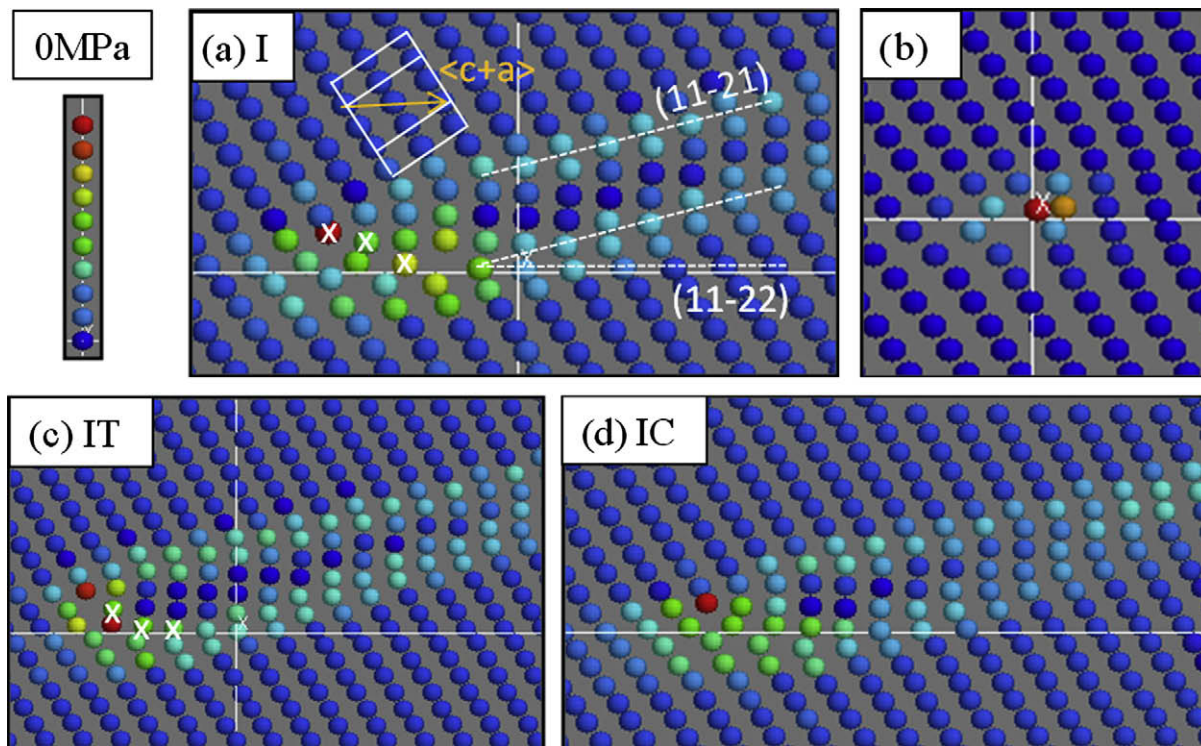


Fig. 6. Edge  $\langle c+a \rangle$  dislocations in the Type I family as predicted for the Sun potential at 0 MPa and 0 K. All cores spread in one  $(11-22)$  plane with a  $(11-21)$  twin embryo: (a) Type I core; (b) Volterra elastic solution; (c) IT core; (d) IC core. Atom colors show potential energy relative to perfect crystal Mg, ranging from  $-0.03$  eV (dark blue) to  $+0.1$  eV (red). (For interpretation of the references to color in this figure legend, the reader is referred to the web version of this article.)

between the yellow atoms. When a negative shear stress is applied on the Type I core, when the stress reaches  $-250$  MPa, it starts moving to the left, leaving behind a line of vacancies (one vacancy every four layers of atoms along the  $[1-100]$  direction), corresponding to the “hole” visible between the yellow atom of the Type I core (Fig. 6a). We denote as IC this new core, shown in Fig. 6d at 0 MPa. This core has a fairly low energy, just  $+0.05$  eV  $b^{-1}$  larger than the IT core energy. It can be formed by removing the red atom of the Volterra elastic solution (Fig. 6b) or by adding an additional row of atom (one atom every four layers of atoms along the  $[1-100]$  direction) just below the two additional basal planes.

The structure and motion of the new low-energy IT core under applied stress are as follows. As the stress is increased above  $+140$  MPa, the twin of the IT core grows progressively, by simultaneously extending on the right, and widens to reach a length of 20 nm and a width of six atomic layers (Fig. 7a) at  $+200$  MPa. At  $+220$  MPa, the entire dislocation with this very extended core glides parallel to the  $(11-22)$  plane. When a negative stress is applied on the IT core, the twin embryo shrinks and the core becomes more compact. At  $-200$  MPa, a Shockley partial is emitted in the basal plane. This partial glides  $\sim 1$  nm, leaving behind a stacking fault to form what we denote as the ITC core (Fig. 7b). The ITC core is stable only between  $-100$  and  $-300$  MPa. For stresses less negative than  $-100$  MPa, it transforms spontaneously back into

the IT core and at  $-300$  MPa a second Shockley is emitted in the basal plane to create a glissile  $\langle a \rangle$  dislocation that glides away and leaves behind a sessile  $\langle c \rangle$  dislocation, as shown in Fig. 7c.

The behavior of the IC core under stress is quite simple. The core glides at  $-160$  MPa and  $+220$  MPa with no significant structural changes during the loading.

The Type III core family is characterized by a spreading in four  $(11-22)$  planes. We obtained the cores in this family, not by applying the Volterra elastic solution, but giving directly “by hand” a V-shape structure to the atom free region ( $\|y\| < b/2$  and  $z < 0$ ) formed to create the edge dislocation, by applying linear displacement such that the defect free zone width vary from  $b = \|\langle c+a \rangle\|$  at  $z = 0$ , to 0 at  $z = -50$  nm. This shape is needed to make the two faces of the atom free region attract each other and the atom free region collapses. After relaxation, a core denoted as Type III' is formed, as shown in Fig. 8a, where the two reds atoms that constitute the extremities of the two extra basal planes of the edge dislocation are separated by 4  $(11-22)$  planes in the  $Z$  direction and by one basal plane along the  $Y = \langle c+a \rangle$  direction. The Type III' core is dissociated into a Shockley partial lying in the basal plane plus a sessile partial and a  $(11-21)$  twin embryo. This core is sessile and has a moderate energy of  $+0.12$  eV  $b^{-1}$  compared to the IT core.

When a positive stress is applied, the Type III' core transforms at  $+140$  MPa into a core we denoted as Type

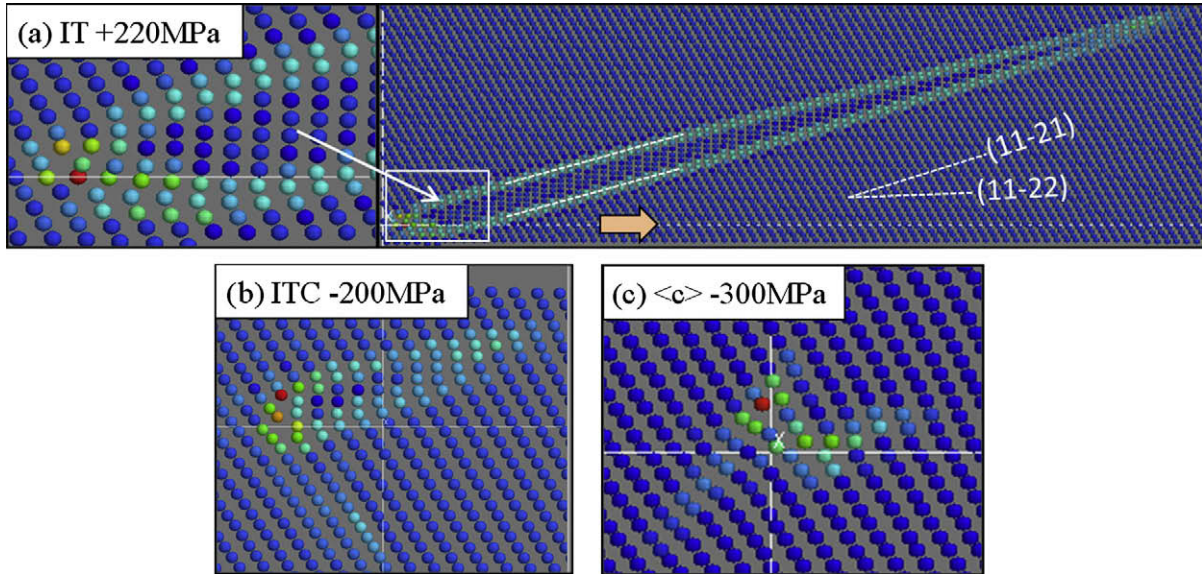


Fig. 7. Edge  $\langle c+a \rangle$  dislocations predicted using the Sun potential at 0 K: (a) IT core at +220 MPa, core detail and wider view showing the 20 nm long  $(11-21)$  twin; (b) ITC core at -200 MPa; (c) Residual  $\langle c \rangle$  dislocation after glide of the  $\langle a \rangle$  dislocation at -300 MPa. Atom colors show potential energy relative to perfect crystal Mg, ranging from -0.03 eV (dark blue) to +0.1 eV (red). (For interpretation of the references to color in this figure legend, the reader is referred to the web version of this article.)

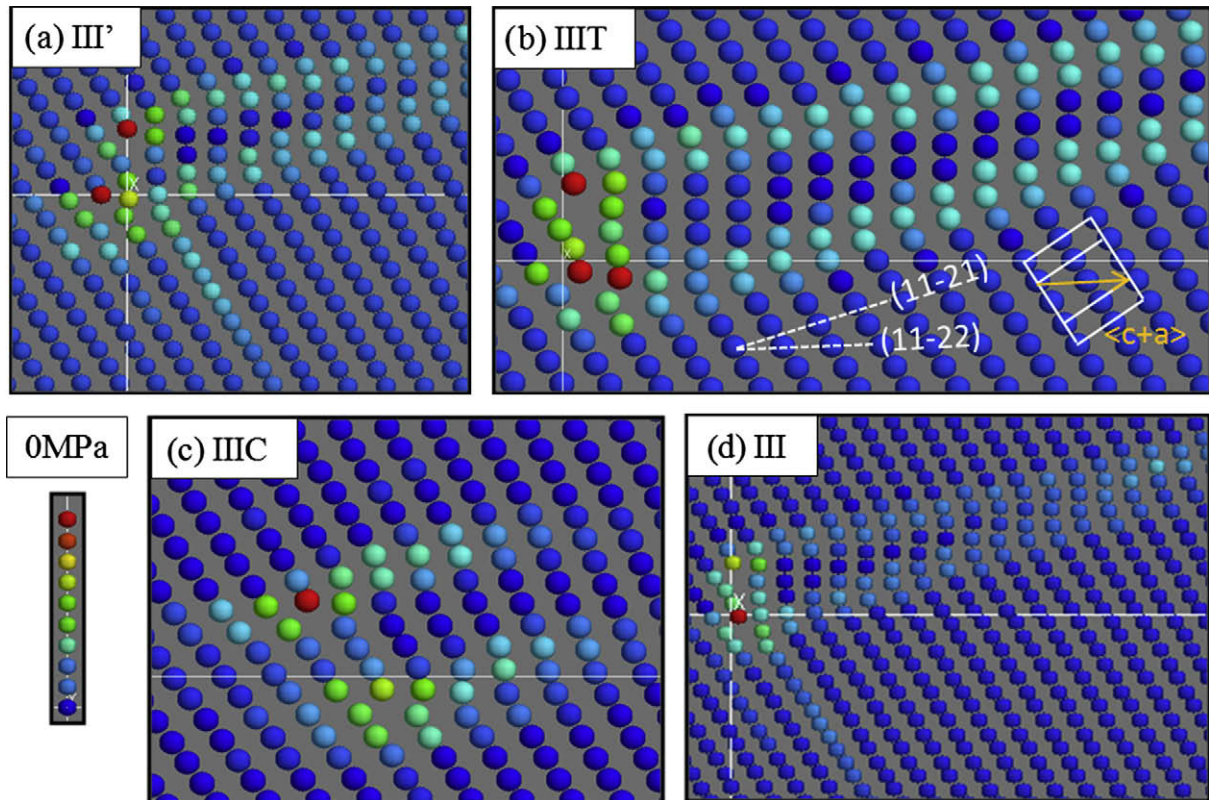


Fig. 8. Edge  $\langle c+a \rangle$  dislocations in the Type III family as predicted using the Sun potential at 0 MPa and 0 K. All cores spread in four  $(11-22)$  planes: (a) Type III'; (b) IIIC core; (c) IIIT core; (d) III core. Atom colors show potential energy relative to perfect crystal Mg, ranging from -0.03 eV (dark blue) to +0.1 eV (red). (For interpretation of the references to color in this figure legend, the reader is referred to the web version of this article.)

IIIT shown in Fig. 8b at 0 MPa, for which the Shockley partial is absorbed into the dislocation core and the lower red atom is shifted to the right, putting the two

extra basal planes side by side. However the extremities of the two extra basal planes are still separated by 4  $(11-22)$  atomic layers in the  $Z$  direction. The IIIT core

has a high energy of  $+0.26 \text{ eV b}^{-1}$  relative to the IT core energy.

The application of a negative stress on the Type III' core pushes the Shockley partial toward the dislocation core and shrinks the  $(1\ 1\ -2\ 1)$  twin embryo. At  $-300 \text{ MPa}$ , as the upper red atoms are shifted to the left, putting the two extra basal planes side by side, the Type III' dislocation transforms into a core we denoted as the Type IIIC, shown in Fig. 8c at  $0 \text{ MPa}$ . The two extra basal plane ends of the IIIC core are also separated by 4  $(1\ 1\ -2\ 2)$  atomic layers, but there is no longer a  $(1\ 1\ -2\ 1)$  twin embryo bounded on these four planes. Rather, two tiny  $(1\ 1\ -2\ 1)$  twin precursors are located on the right of the ends of the extra basal planes. The Type IIIC core has a high energy of  $+0.26 \text{ eV b}^{-1}$  relative to the IT core.

Under stress, the Type IIIT core evolves as follows. At  $+220 \text{ MPa}$ , the  $(1\ 1\ -2\ 1)$  twin embryo of the IIIT core extends and grows up to eight layers before reaching the surface of the sample, as seen Fig. 9a. In contrast to the IT core, its left part remains sessile. It seems that this difference is due to the fact that the IIIT core spreads on 4  $(1\ 1\ -2\ 2)$  layers whereas the IT core spreads in only one  $(1\ 1\ -2\ 2)$  plane where it can glide. When a negative stress is applied to the IIIT core, it transforms at  $-40 \text{ MPa}$  into the sessile Type III core shown in Fig. 8d at  $0 \text{ MPa}$ . This core is very similar to the Type III' core except that the red and the yellow atoms that constitute the extremities of the two extra basal planes are no longer separated by an extra basal plane. Applying a stress to the Type IIIC core leads to glide at  $-160 \text{ MPa}$  and transformation into the Type IIIT core at  $+140 \text{ MPa}$ .

The Type III core has a low energy, just  $+0.02 \text{ eV b}^{-1}$  larger than the IT core. The Type III core was obtained by applying  $+100 \text{ MPa}$  to the III' core so that it transforms into the IIIT core, then  $-40 \text{ MPa}$  to this IIIT core that transforms into the Type III core. When a negative stress is applied to the III core, the second Shockley partial is emitted at  $-300 \text{ MPa}$ , as for ITC. Thus, the created  $\langle a \rangle$  dislocation glides away and leaves behind a sessile  $\langle c \rangle$  dislocation. When a positive stress is applied, the Type III core transforms at  $+100 \text{ MPa}$  into the IIIT core.

The main results for edge dislocations as found using the Sun et al. potential are summarized in Table 2, which

Table 3

Edge  $\langle c+a \rangle$  dislocation for the Liu potential: transformations and CRSS at  $0 \text{ K}$ .

Core	$E-E_{IT}$ ( $\text{eV b}^{-1}$ )	Negative CRSS (MPa)		Positive CRSS (MPa)	
Type I	+0.29	-80	→IT	+200	→IT
Type IC	+0.06	-80	Glide	+140	Glide
Type IT	0.00	-280	Glide	+220	Glide
Type III	+0.03	-160	→IIIC	+200	→IIIT
Type IIIT	-	-	-	+300	Glide
Type IIIC	+0.19	-140	Glide	+200	Glide

shows the core energies, and the critical resolved shear stresses for either glide or transformation.

For the Liu et al. potential, the same types of edge cores can be observed but some differences relative to the Sun potential are found, both in the mechanisms and Peierls stresses. All dislocation cores glide or transform into glissile cores and no twinning is observed up to the Peierls stress calculated. In particular, with the Liu potential, Type III' core is not stable and transforms into Type III core at  $0 \text{ MPa}$ . For positive stresses the III core transforms into the IIIT core at  $+200 \text{ MPa}$  as compared to  $+100 \text{ MPa}$  for the Sun potential, the IIIT core does not twin but rather glides at  $+300 \text{ MPa}$ , while the IIIC does not transform into the IIIT core but glides at  $+200 \text{ MPa}$ . For negative stresses, the Type I core does not transform into the IC core but into the IT core at  $-80 \text{ MPa}$ , the IT core does not dissociate into  $\langle c \rangle$  and  $\langle a \rangle$  dislocations but glides at  $-280 \text{ MPa}$ , while the IC core glides at  $-80 \text{ MPa}$  as compared to  $-160 \text{ MPa}$  for the Sun potential. A summary of results obtained for edge dislocations using the Liu potential is given in Table 3.

### 5. $\langle c + a \rangle$ Dislocations at finite temperature

We have calculated the Peierls stresses under positive shear stress as a function of temperature for the most glissile screw and edge cores, e.g. pyramidal I PI and pyramidal II IT. The results are given in Table 4. The Peierls stresses drop by 30–40% at  $5 \text{ K}$ , and by 97% at  $300 \text{ K}$ , where they are below  $\pm 5 \text{ MPa}$ . Dislocation glide changes from kink motion to fcc like motion. At  $300 \text{ K}$ , since the

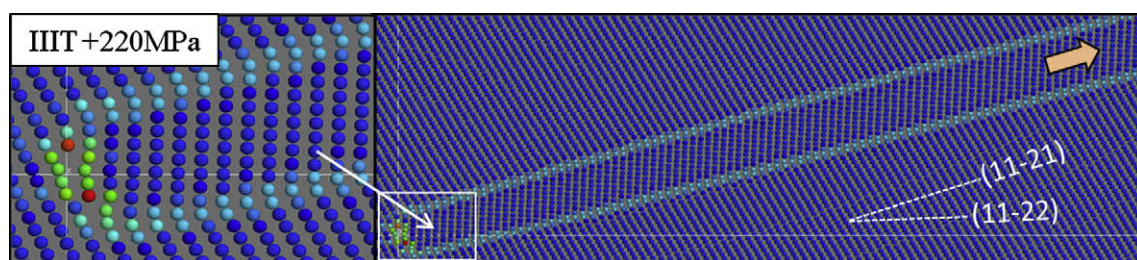


Fig. 9. Edge  $\langle c + a \rangle$  IIIT core as predicted by the Sun potential at  $+220 \text{ MPa}$  and  $0 \text{ K}$ , showing the formation of an extended  $(1\ 1\ -2\ 1)$  twin. Atom colors show potential energy relative to perfect crystal Mg, ranging from  $-0.03 \text{ eV}$  (dark blue) to  $+0.1 \text{ eV}$  (red). (For interpretation of the references to color in this figure legend, the reader is referred to the web version of this article.)

Table 4  
CRSS vs. temperature for screw  $\{1-101\}$  PI and edge  $\{11-22\}$  IT  $\langle c+a \rangle$  dislocations.

Temperature (K)		0	5	77	150	200	300
CRSS (MPa)	Edge $\{11-22\}$ IT	+220	+130	+115	+60	+30	+5
	Screw $\{1-101\}$ PI	+80	+55	+29	+13	+5	+2.5

Peierls stresses are low, the dislocation cores have the same structure as the cores at 0 MPa at 0 K, even when they glide.

At 300 K, the screw  $\langle c+a \rangle$  dislocation  $\{1-101\}$  PI glides for low stresses,  $-5$  MPa and  $+2.5$  MPa for positive and negative applied stresses, whereas the dislocation  $\{1-100\}$  P0 glides for larger stresses,  $-50$  MPa and  $+50$  MPa. The  $\{11-22\}$  PII dislocation transforms into  $\{1-101\}$  PI dislocation for negative and positive stresses of  $-30$  MPa and  $+30$  MPa, respectively. The  $\{11-21\}$  P0 dislocation transforms similarly into  $\{1-101\}$  PI at stresses  $-85$  MPa and  $+60$  MPa; then, if the stress is kept on increasing, the  $(-12-11)$  twin embryo of the  $\{1-101\}$  PI dislocation extends more and more, and finally  $(-12-11)$  twinning is observed at  $+150$  MPa, as observed at 0 K under  $+280$  MPa. These results are summarized in Table 2.

At 300 K and positive stresses, the edge  $\langle c+a \rangle$  IT dislocation glides at  $+2.5$  MPa, whereas the IC core glides at a higher stress of  $+27$  MPa, while for negative stresses both glide at  $-27$  MPa. Despite its relatively high energy, the IIIC core is stable at 300 K and it is able to glide in both direction for stresses of  $\pm 45$  MPa. However, under positive stress, the IIIC core seems to start to transform the same way as 0 K while gliding. The high energy I core becomes unstable at 200 K where it transforms also into the IT core. The IIIT core, despite having the same energy as IIIC, becomes unstable at 250 K and transforms into the lowest energy IT core. The Type III and III' cores are stable at 300 K. The Type III core transforms into the lowest energy IT core at stresses of  $-90$  MPa and  $+40$  MPa. The Type III' core also transforms into the core IT at  $+40$  MPa, but for negative stresses it dissociates into  $\langle c \rangle$  and  $\langle a \rangle$  dislocations at  $-300$  MPa. The results for edge  $\langle c+a \rangle$  dislocation at 300 K are summarized in Table 2.

## 6. Discussion and conclusions

Our study here shows notable differences as compared to previous simulations at 0 K. In the previous simulations [1,3,8–13], PI and PII screw and Type I, II and III edge cores were observed, whereas we did not observe the Type II edge core and found a new P0 screw core and new IC, IT, IIIC, IIIT and III' edge cores. The behavior of dislocations under applied stresses also differs between this work and the prior work. Prior studies observed that screw PI  $\langle c+a \rangle$  dislocation glides in the pyramidal I plane for positive stresses but in the pyramidal II plane for negative stresses,

whereas we find that PI core glides in pyramidal I for both positive and negative stresses. Prior work showed that the edge  $\langle c+a \rangle$  Type I core transforms into a Type II core for negative stresses and twins for positive stresses, whereas we find Type I transforms into Type IC core for negative stresses and into IT core for positive stresses that are both glissile cores. For both negative and positive stresses, the Type II core was glissile and the Type III core was sessile, whereas we find that Type III core dissociates into a  $\langle c \rangle$  and  $\langle a \rangle$  dislocations for negative stresses and transforms into the twinning Type IIIT core for positive stresses. All these differences of core stabilities and properties, especially the presence of the Type II core, may be due to the characteristics of the previous potentials that were aimed at modeling Zr and exhibited a more stable SF in the  $(11-22)$  plane, as well as to the small simulation sizes, the boundary conditions, and the imposed strain increments used in previous simulations. Regarding artifacts due to simulation cell size and loading, for instance, we are able to observe twinning for the edge  $\langle c+a \rangle$  dislocations that have a long  $\{11-21\}$  twin embryo when using a smaller simulation cell (40 nm) and a larger stress increment (20% of the Peierls stress).

Differences with previous simulations using a Zr Lennard–Jones potential [11] are also observed at finite temperature. In those 2D simulations in a very small simulation cell (glide distance about 3 times the dislocation spreading), the Type III edge  $\langle c+a \rangle$  dislocation did not move even for  $\pm 10\%$  strain, at 30 K. The screw dislocation core, spread on two  $\{1-101\}$  planes with a V shape at 0 K, started to spread in the  $\{11-22\}$  plane at 300 K and spread entirely in this plane at 1000 K. At 300 K, the screw core glided at  $+0.015$  and  $-0.02$  strains in pyramidal II plane, and underwent numerous double cross-slips. We observe none of these behaviors.

The screw  $\langle c+a \rangle$  dislocations glide in the pyramidal planes at  $-140/+80$  MPa at 0 K and  $-5/+2.5$  MPa at 300 K, whereas they glide at larger stresses in the prism plane,  $\pm 200$  MPa at 0 K and  $\pm 50$  MPa at 300 K, which is in qualitative agreement with experiments in hcp where  $\langle c+a \rangle$  dislocations glide in the pyramidal planes, and not in prism plane. However, our studies predict glide in the pyramidal I plane for Mg whereas slip lines observed on sample surfaces and TEM observations indicate glide in the pyramidal II plane [24–28]. However our predicted glide in the pyramidal I plane versus glide in the pyramidal II plane correlates well with the relative values of the maximum unstable stacking fault energy along the  $1/3 \langle 11-23 \rangle$  minimum energy path between the pyramidal I and II planes, for both Sun and Liu EAM potentials and for the ab initio calculations. An explanation for the  $\{11-22\}$  glide observed in experiments might be that the dislocation glide is accommodated on average along the  $(11-22)$  plane by successive double cross-slips between the  $(01-1-1)$  and the  $(10-1-1)$  planes. However, this remains speculation; we did not observe double cross-slip in our MD simulations, which do not provide

the time needed for thermally activated events such as cross-slip. Also, the double cross-slip glide explanation could explain experiments at 300 K where the coarse slip lines indicate numerous cross-slips, but not at 77 K where well defined slip lines show that double cross-slip is unlikely. Thus, the discrepancy between simulations and experiments remains to be explained.

We have not addressed the formation mechanisms or sources of  $\langle c + a \rangle$  dislocations. A simple mechanism for formation of the P0 screw  $\langle c + a \rangle$  dislocation core would be via cross-slip of a basal  $\langle a \rangle$  screw into the prism plane followed by reaction with a sessile prism screw  $\langle c \rangle$  dislocation. Then, since the P0 Peierls stress in the prism plane is larger than the PI Peierls stress in the pyramidal I plane, the P0 could cross-slip onto the pyramidal I plane and transform into a PI core [13]. Another possible mechanism for formation of an edge  $\langle c + a \rangle$  Type III dislocation would be via the recombination of a glissile basal edge  $\langle a \rangle$  dislocation that reacts with a sessile prism edge  $\langle c \rangle$  dislocation, which is the opposite of the reaction observed here when the Type III edge  $\langle c + a \rangle$  core dissociates into a  $\langle c \rangle$  and a  $\langle a \rangle$  dislocations under a high applied stress of  $-300$  MPa. These hypotheses have yet to be tested by molecular simulations.

At 0 K, we observe glissile edge  $\langle c + a \rangle$  dislocation cores (Types IC, IT and IIIC) laying in pyramidal II plane and sessile cores partially dissociated in the basal plane (Types III and III') in agreement with experiments [24–28], but also  $\{11-21\}$  twins in tension, in disagreement with experiments where the tension twins are the  $\{1-102\}$  twins [29]. However, these  $\{11-21\}$  twins are due to the high dislocation glide CRSS at 0 K and disappear in simulations at finite temperature, where the CRSSs drop significantly from hundreds of MPa to tens of MPa. The most stable edge  $\langle c + a \rangle$  is the IT core. At 300 K all the different cores, except IIIC and III' for negative stresses, transform into the IT core. This core glides for stresses as small as  $-27$  and  $+5$  MPa, which is less than the 40 MPa usually reported in the literature [25,28]. The higher experimental value may be due to the presence of impurities even at very low concentration. The higher experimental value may also indicate the higher stresses required to transform the sessile Type III cores into glissile IT cores. Such a mechanism could explain the plastic instabilities near the yield point observed at low temperature on the Mg stress–strain curves [28]. Finally, the EAM potential may not represent the Peierls energy barrier versus applied stress sufficiently well to capture the variation in thermal activation with temperature.

In experiments, yield stress increases with temperature by 50–60% between 150 K and 300 K [24–29]. In previous modeling work at 0 K [10–13], this phenomenon was explained by the mechanism of edge  $\langle c + a \rangle$  dislocation trapping due to the transformation of glissile  $\langle c + a \rangle$  cores into sessile Type III cores that had a lower energy. However, in our simulations using improved potentials for Mg [16], the lowest energy core is the glissile core IT, and

not the sessile Type III core. Thus, there is no driving force for the transformation IT  $\rightarrow$  III, and so the previous explanation does not apply.

In conclusion, the gamma surfaces in the pyramidal I ( $1-101$ ) and II ( $11-22$ ) planes calculated with Sun and Liu potentials are in reasonable agreement with those obtained by ab initio calculations. At 0 K, screw  $\langle c + a \rangle$  dislocations glide in the  $\{1-101\}$  pyramidal plane I for  $-140/+80$  MPa and in the prism plane for larger stresses ( $\pm 200$  MPa), but not in the  $\{11-22\}$  pyramidal II plane observed in experiments. However, this preferred glide in the pyramidal I compared to the pyramidal II plane correlates well with the calculated gamma surfaces. At 300 K, the PI screw core glides in the pyramidal I plane for stresses below  $-5/+2.5$  MPa, and the P0 core glides in the prism plane for  $\pm 50$  MPa. New glissile low energy edge  $\langle c + a \rangle$  dislocation cores were observed in addition of the sessile Type I and Type III cores observed in previous simulations, but the Type II core was not observed. At 0 K, for negative stresses, we observed either dislocation glide (starting with I, IC, III' or IIIC cores) or dissociation into  $\langle c \rangle$  and  $\langle a \rangle$  dislocations (starting with IT, III or IIIT cores). For positive stresses, we obtained either dislocation glide (starting with Type I family cores that spread on one  $(11-22)$  plane) or twinning (starting with Type III family cores that spread on 4  $(11-22)$  planes). The lowest energy core is the glissile IT core, not the sessile Type III core as reported in previous simulations. At 300 K, under applied stress, all the edge  $\langle c + a \rangle$  cores but two transform into the IT core, which then glides for stresses below  $-27/+5$  MPa. Thus, both screw and edge  $\langle c + a \rangle$  dislocations were found to glide for low stresses at 300 K. However,  $\langle c + a \rangle$  dislocation is only one part of the problem of deformation mechanisms to accommodate the deformation along  $\langle c \rangle$  axis, and is often competed by twinning. Our future work will address the question of twinning in Mg.

## Acknowledgements

TN and WAC are supported through the General Motors/Brown Collaborative Research Laboratory on Computational Materials Science. WAC acknowledges additional support from the NSF MRSEC at Brown University (NSF Grant DMR-0520651). The work of JAY and DRT is supported by the NSF GOALI program, Grant 0825961, and with support from General Motors. Computational resources for ab initio calculations were provided by a grant from Intel, and in part by the NSF through TerraGrid resources provided by NCSA.

## References

- [1] Minonishi Y, Ishioka S, Koiwa M, Morozumi M, Yamaguchi M. *Phil Mag A* 1981;43:1017.
- [2] Minonishi Y, Ishioka S, Koiwa M, Morozumi M, Yamaguchi M. *Philos Mag A* 1981;44:1225.
- [3] Minonishi Y, Ishioka S, Koiwa M, Morozumi M, Yamaguchi M. *Philos Mag A* 1982;45:835.

- [4] Minonishi Y, Ishioka S, Koiwa M, Morozumi M. *Philos Mag A* 1982;46:761.
- [5] Numakura H, Minonishi Y, Koiwa M. *Philos Mag A* 1990;62(5):545.
- [6] Numakura H, Minonishi Y, Koiwa M. *Philos Mag A* 1990;62(5):525.
- [7] Liang MH, Bacon DJ. *Philos Mag A* 1986;53:163.
- [8] Liang MH, Bacon DJ. *Philos Mag A* 1986;53:181.
- [9] Liang MH, Bacon DJ. *Philos Mag A* 1986;53:205.
- [10] Ando S, Takashima K, Tonda H. *Mater Trans JIM* 1996;37(3):319.
- [11] Ando S, Gotoh T, Tonda H. *Metall Mater Trans A* 2002;33(3):823.
- [12] Morris JR, Ho KM, Chen KY, Rengarajan G, Yoo MH. *Model Simul Mater Sci Eng* 2000;8:25.
- [13] Yoo MH, Morris JR, Ho KM, Agnew SR. *Metall Mater Trans A* 2002;33:813.
- [14] Liu X-Y, Adams JB, Ercolessi F, Moriarty JA. *Model Simul Mater Sci Eng* 1996;4:293.
- [15] Sun DY, Mendeleev MI, Becker CA, Kudin K, Haxhimali Tomorr, Asta M, et al. *Phys Rev B* 2006;73:024116.
- [16] Yasi JA, Nogaret T, Trinkle DR, Qi Y, Hector Jr LG. *Model Simul Mater Sci Eng* 2009;17:055012.
- [17] Plimpton S. *J Comp Phys* 1995;117(1):1.
- [18] Kresse G, Hafner J. *J Phys Condens Matter* 1994;6:8245.
- [19] Kresse G, Furthmüller J. *Phys Rev B* 1996;54:11169.
- [20] Vanderbilt D. *Phys Rev B* 1990;41:7892.
- [21] Kresse G, Hafner J. *Phys Rev B* 1993;47:558.
- [22] Perdew JP, Wang Y. *Phys Rev B* 1992;45:13244.
- [23] Bitzek E, Koskinen P, Gahler F, Moseler M, Gumbusch P. *Phys Rev Lett* 2006;97:170201.
- [24] Stohr JF, Regnier P, Dupouy JM. *Mem Sci Rev Metall* 1971;LXVIII(1):49.
- [25] Stohr JF, Regnier P. *Philos Mag* 1971;25:1313.
- [26] Obara T, Yoshinga H, Morozumi S. *Acta Metall* 1973;21:845.
- [27] Ando S, Tonda H. *Mater Trans JIM* 2000;41(9):1188.
- [28] Tonda H, Ando S. *Metall Mater Trans A* 2002;33:831.
- [29] Agnew SR, Horton JA, Yoo MH. *Metall Mater Trans A* 2002;33:851.